Monthly Notices
of the
ROYAL ASTRONOMICAL SOCIETY

MNRAS **468,** 4579–4591 (2017)
Advance Access publication 2017 April 1

doi:10.1093/mnras/stx788

The galaxy population in cold and warm dark matter cosmologies

Lan Wang,[1⋆] Violeta Gonzalez-Perez,[2,3] Lizhi Xie,[4] Andrew P. Cooper,[2] Carlos S. Frenk,[2] Liang Gao,[1] Wojciech A. Hellwing,[3,5] John Helly,[2] Mark R. Lovell[6,7] and Lilian Jiang[2]

[1]*Key Laboratory for Computational Astrophysics, National Astronomical Observatory, Chinese Academy of Sciences, Datun Road 20A, Beijing 100012, China*
[2]*Institute for Computational Cosmology, Department of Physics, University of Durham, South Road, Durham DH1 3LE, UK*
[3]*Institute of Cosmology and Gravitation, University of Portsmouth, Burnaby Road, Portsmouth PO1 3FX, UK*
[4]*INAF – Astronomical Observatory of Trieste, via G.B. Tiepolo 11, I-34143 Trieste, Italy*
[5]*Janusz Gil Institute of Astronomy, University of Zielona Góra, ul. Szafrana 2, PL-65-516 Zielona Góra, Poland*
[6]*GRAPPA, Universiteit van Amsterdam, Science Park 904, NL-1098 XH Amsterdam, the Netherlands*
[7]*Instituut-Lorentz for Theoretical Physics, Niels Bohrweg 2, NL-2333 CA Leiden, the Netherlands*

Accepted 2017 March 28. Received 2017 March 27; in original form 2016 December 11

ABSTRACT

We use a pair of high-resolution *N*-body simulations implementing two dark matter models, namely the standard cold dark matter (CDM) cosmogony and a warm dark matter (WDM) alternative where the dark matter particle is a 1.5 keV thermal relic. We combine these simulations with the GALFORM semi-analytical galaxy formation model to explore differences between the resulting galaxy populations. We use GALFORM model variants for CDM and WDM that result in the same $z = 0$ galaxy stellar mass function by construction. We find that most of the studied galaxy properties have the same values in these two models, indicating that both dark matter scenarios match current observational data equally well. Even in underdense regions, where discrepancies in structure formation between CDM and WDM are expected to be most pronounced, the galaxy properties are only slightly different. The only significant difference in the local universe we find is in the galaxy populations of 'Local Volumes', regions of radius 1–8 Mpc around simulated Milky Way analogues. In such regions, our WDM model provides a better match to observed local galaxy number counts and is five times more likely than the CDM model to predict subregions within them that are as empty as the observed Local Void. Thus, a highly complete census of the Local Volume and future surveys of void regions could provide constraints on the nature of dark matter.

Key words: galaxies: abundances – galaxies: formation – galaxies: high-redshift – dark matter.

1 INTRODUCTION

Most matter in the Universe is made of unknown exotic fundamental particles known as dark matter. Its existence has been inferred from various observations, including galaxy rotational curves, gravitational lensing and the mass-to-light ratio of clusters (see a recent review by Bertone & Hooper 2016). The most popular model of dark matter consists of a supersymmetric particle that has a negligible velocity dispersion, allowing density perturbations imprinted in the early Universe to persist down to very small scales. This model is successful in matching a large body of observations, from temperature fluctuations in the microwave background (e.g. Komatsu et al. 2011; Planck Collaboration XI 2016) to the galaxy distribution today (e.g. Frenk & White 2012; Sánchez et al. 2017). Nevertheless, there has been growing controversy about its validity on the scale of individual galaxies and below. For example, it has been suggested that there are discrepancies between predictions and observations of the abundance of satellite galaxies around the Milky Way (Klypin et al. 1999; Moore et al. 1999), of the kinetic stellar data of the Milky Way satellites (Boylan-Kolchin, Bullock & Kaplinghat 2012) and of the density profiles of low surface brightness dwarf galaxies (Moore et al. 1999; Springel et al. 2008).

The most popular candidate for cold dark matter (CDM) – the hypothetical weakly interacting massive particle (WIMP) – has not been detected despite a dedicated campaign of searches in colliders, underground laboratories (Akerib et al. 2014) and the gamma-ray sky (e.g. Ackermann et al. 2015). It is therefore imperative to consider alternative dark matter candidates such as, for example, the keV-scale gravitino or sterile neutrino. In addition to their specific

⋆ Email: wanglan@bao.ac.cn

particle physics identities, these two candidates differ from WIMPs in that they are warm dark matter (WDM) candidates rather than CDM ones.

The WDM model has been considered to be one possibility for solving the issues facing the CDM cosmology on small scales. In the past decade, many papers have modelled WDM structure formation (e.g. Bode, Ostriker & Turok 2001; Knebe et al. 2002, 2003; Busha, Evrard & Adams 2007; Colín, Valenzuela & Avila-Reese 2008; Zavala et al. 2009; Smith & Markovic 2011; Lovell et al. 2012, 2014; Schneider et al. 2012; Angulo, Hahn & Abel 2013; Benson et al. 2013; Destri, de Vega & Sanchez 2013; Kamada et al. 2013; Bose et al. 2016; Li et al. 2016, 2017; Ludlow et al. 2016). In the WDM model, the dark matter particles have intrinsic thermal velocities, and these velocities influence the small-scale structure formation of the Universe mainly in two different ways. First, the motion of WDM particles would quench the growth of structure below some free-streaming scale (the distance over which a typical WDM particle travels). Since small and dense haloes do not form below the free-streaming-scale, the dark matter haloes that surround galaxies in a WDM model have far less substructure compared to their CDM counterparts, which may help alleviate the satellite abundance problem (Bode et al. 2001). Secondly, according to the phase-space density theory (Tremaine & Gunn 1979), the primordial velocities of collisionless WDM particles impose a finite phase-space density, which ultimately prevents the formation of a cuspy profile in WDM haloes (Shao et al. 2013). Consequently, the innermost density profiles of WDM haloes are predicted to be cored instead of the cuspy ones predicted by CDM simulations. Nevertheless, recent progress on understanding the density profile of WDM haloes indicates that a realistic warm dark model cannot account for the sizes of cores in the density profiles of dwarf galaxies inferred from observations (Macciò et al. 2013; Shao et al. 2013). The observed sizes of cores of dwarf galaxies (Gilmore et al. 2007; Walker & Peñarrubia 2011) should be produced by some baryonic physics, such as outflows (Navarro, Eke & Frenk 1996), supernovae feedback and baryon clumps (Del Popolo & Pace 2016), or reflect a different dark matter candidate such as self-interacting dark matter (Vogelsberger, Zavala & Loeb 2012; Zavala, Vogelsberger & Walker 2013).

To explore baryonic physics in WDM cosmogonies, studies of galaxy formation have been carried out by using either semi-analytic models (Menci, Fiore & Lamastra 2012, 2013; Kang, Macciò & Dutton 2013; Nierenberg et al. 2013; Lovell et al. 2016,b; Bose et al. 2017), or hydrodynamical simulations (Herpich et al. 2014; Colín et al. 2015; Maio & Viel 2015; Lovell et al. 2016c; Power & Robotham 2016). These works have studied observables including global galaxy properties like luminosity/stellar mass functions and galaxy colour/star formation (Menci et al. 2012, 2013; Kang et al. 2013; Herpich et al. 2014), the inner structure of galaxies (Herpich et al. 2014; Colín et al. 2015; González-Samaniego, Avila-Reese & Colín 2016; Power & Robotham 2016) and the properties of satellite galaxies around galaxies comparable to the Milky Way (Nierenberg et al. 2013; Lovell et al. 2016,b). The masses of the WDM particles adopted in these studies vary from $m_x = 0.5$ to 3.3 keV. These values were inferred from constraints provided by different observations: the numbers of Milky Way satellites (Polisensky & Ricotti 2010), X-ray observations of the Andromeda galaxy (Watson, Li & Polley 2012), galaxy counts at high redshift (Pacucci, Mesinger & Haiman 2013), high redshift long γ-ray bursts (de Souza et al. 2013) and the high-redshift Ly α forest data (Viel et al. 2013).

In this work, we present two simulations, one in a CDM and the other in a WDM cosmogony. The two simulations have identical initial conditions, except for a truncation on small scales in the power spectrum of the WDM simulation. Our simulations are state-of-the-art in both the volume of the universe they simulate and their mass resolution. We exploit these advantages by combining the two simulations with GALFORM, a semi-analytic model of galaxy formation. This allows us to explore systematic differences between the galaxy populations formed in the two cosmologies. Historically, cosmological WDM simulations, and hence semi-analytic galaxy formation models built on them, have suffered from uncertainties introduced by spurious self-bound DM clumps arising from numerical discreetness effects (Wang & White 2007). These spurious haloes have been carefully removed from the halo catalogue on which our galform model is based by applying the procedure of Lovell et al. (2014), which improves the reliability of comparisons between our results and observations. We note that hydrodynamical simulations by Gao & Theuns (2007) and Gao, Theuns & Springel (2015) have demonstrated a novel star formation mechanism in WDM, which occurs in filaments rather than in collapsed dark matter haloes. Estimates of the star formation efficiency of this process are currently highly uncertain, however, so we neglect it in this study.

The outline of our paper is as follows. In Section 2, we introduce our simulation sets and the semi-analytic models used to populate dark matter haloes with galaxies. In Section 3, we study the statistics of galaxy properties at both low and high redshifts. In Section 4, we compare the properties of voids and their constituent galaxies, because the differences between WDM and CDM cosmogonies are expected to be most pronounced in these low-density regions. Finally, we present a discussion and our conclusions in Section 5.

2 SIMULATIONS AND GALAXY FORMATION MODELS

2.1 Simulations

The numerical simulations used in this study comprise a pair of high-resolution dark matter-only simulations. The two simulations are identical except for the different nature of dark matter, one with standard CDM and one with a WDM model. The former one has been introduced in detail by Hellwing et al. (2016). For each of the simulations, 1620^3 particles are evolved within a box of length 100 Mpc on a side. Thus, the individual particle mass is $6.2 \times 10^6\,\mathrm{M}_\odot$. Cosmological parameters consistent with the *WMAP7* results (Komatsu et al. 2011) are adopted. The details of the simulation setup and cosmological parameters are presented in Table 1.

The initial conditions for the simulations are generated at redshift $z = 127$, made by a 3072^3 Fourier grids with initial phases taken from the multiscale Gaussian field called Panphasia (see Jenkins 2013, for details). The transfer function of the CDM run is computed with the Boltzmann code CMBFAST (Seljak & Zaldarriaga 1996). For the WDM run, the linear power spectrum is calculated by sharply truncating (Viel et al. 2005) the CDM power below a free-streaming scale corresponding to that of 1.5 keV relic particle. This choice of WDM particle mass is warmer than the latest Ly α forest constraint allows (Viel et al. 2013; Garzilli, Boyarsky & Ruchayskiy 2015). This model is used because it is extreme, and therefore emphasizes the differences between CDM and WDM cosmologies. Note that the two simulations use the same random phase to initialize the Gaussian fields, allowing a straightforward comparison between the two dark matter models.

Table 1. The details of the two simulations used in this study. L is the side length of the simulation box; N is the total number of particles; $m_{\rm dm}$ is the particle mass; ϵ is the force softening length; $m_{\rm WDM}$ is the assumed mass of the thermal WDM particle in the WDM simulation. Cosmological parameters are consistent with the *WMAP7* results (Komatsu et al. 2011). $\Omega_{\rm m}$, Ω_Λ and $\Omega_{\rm b}$ are, respectively, the cosmological average densities of matter, dark energy and baryonic matter in units of the critical density at redshift zero. H_0 is the Hubble parameter. σ_8 is the square root of the linear variance of matter distribution when smoothed with a top-hat filter of radius $8\,h^{-1}$ Mpc.

Property	Value
L (comoving h^{-1} Mpc)	70.4
N	1620^3
$m_{\rm dm}$ ($h^{-1}\,{\rm M}_\odot$)	6.20×10^6
ϵ (comoving h^{-1} kpc)	1.0
$m_{\rm WDM}$ (keV, for the WDM simulation)	1.5
$\Omega_{\rm m}$	0.272
Ω_Λ	0.728
$\Omega_{\rm b}$	0.044 55
$h \equiv H_0/(100\ {\rm km\ s^{-1}\ Mpc^{-1}})$	0.704
σ_8	0.81
n	0.967

The simulations are performed with the GADGET-3 Tree-PM N-body code, which is an updated version of the public GADGET-2 code (Springel 2005). For each simulation, we have record 80 snapshots roughly logarithmically spaced in redshift between $z = 40$ and 0.

For each output snapshot, dark matter haloes are identified using a Friends-Of-Friends (FOF) algorithm (Davis et al. 1985) with a linking length of $b = 0.2$ in units of the mean interparticle separation. Then the SUBFIND algorithm (Springel et al. 2001) is applied to identify self-bound and locally overdense substructures within each FOF halo. Substructures with more than 20 particles are considered as subhaloes. Halo/subhalo merger trees are constructed following the method described by Jiang et al. (2014).

WDM simulations are affected by numerical discreetness, which causes artificial fragmentation of the smooth filaments. This results in an effective halo mass resolution limit (Wang & White 2007) of $2.42 \times 10^9\,h^{-1}\,{\rm M}_\odot$ in our WDM simulation, below which most structures identified by our halo finder are spurious (see Appendix A and Fig. A1). Some of the spurious haloes are massive enough that gas condenses and forms stars within them, which would affect the predictions of semi-analytic modelling even above this mass limit. We therefore follow the method described in Lovell et al. (2014) to carefully identify and remove these spurious haloes from the halo merger trees.

Hereafter we refer to the simulation with CDM as COLOR (COco LOw Resolution simulation).[1] We refer to the simulation with WDM of mass $m_x = 1.5$ keV as COLOR-WARM (this is identical to the simulation 'COLOR-1.5' in Ludlow et al. 2016).

2.2 Model galaxies

The semi-analytic galaxy formation model used in this study is the GALFORM model described by Gonzalez-Perez et al. (2014, hereafter GP14[2]), which builds on an earlier work by Cole et al. (2000), Bower et al. (2006) and Lagos et al. (2012). The GP14 model was calibrated on the MS-W7 simulation (Guo et al. 2013; Lacey et al. 2016), which adopts the same *WMAP7* cosmology as the simulations used in this work but has a much larger volume $(500\,h^{-1}\,{\rm Mpc})^3$ and a lower mass resolution of $9.35 \times 10^8\,h^{-1}\,{\rm M}_\odot$. The GP14 model successfully reproduces a wide range of observations (GP14; Lagos et al. 2015; Merson et al. 2016).

The physical and numerical parameters of a semi-analytical model such as GP14 are typically calibrated with reference to a particular set of simulation merger trees. The particle mass resolution, the time resolution and (more physically) the mass assembly histories of DM haloes in a particular cosmogony, all influence the predicted properties of galaxies to some degree (Lee et al. 2014). GALFORM includes numerical prescriptions intended to ensure that the properties of galaxies well resolved in the simulation used for calibration are converged with respect to further increases in mass and time resolution. We nevertheless find that direct application of the original GP14 model to the COLOR simulation results in global statistics for the galaxy population that are slightly different from those obtained in the MS-W7 calibration (e.g. the stellar mass function; see Fig. 1). We attribute this primarily to sample variance (COLOR has a volume 358 times smaller than that of MS-W7); this issue is addressed in detail in Appendix B.

In order to mitigate effects of these differences between CDM and WDM galaxy properties, we recalibrate the parameters of the model we apply to the COLOR-WARM simulation such that they yield the same $z = 0$ galaxy stellar mass function as the original GP14 model applied to COLOR (in the mass range $10^9 < M_{\rm stars}/(h^{-1}\,{\rm M}_\odot) < 10^{11}$). We refer to this WDM-based recalibration of the model as Re-GP14. This recalibration introduces minimal changes to parameters controlling the strength of supernovae feedback (relatively weaker than GP14 in low-mass galaxies) and AGN feedback – full details are given in Appendix C. We stress that we have *not* altered the parameters of the original GP14 model that we apply to COLOR. Consequently, our comparison is built on two models that make essentially identical predictions for the distribution of galaxy masses in the simulation box, but which employ slightly different models of baryonic physics to achieve this (due to effects of differences in structure formation between CDM and WDM).

On this basis, in the following sections, we explore how other galaxy properties differ between the two models: the original GP14 model applied to the COLOR simulation and the Re-GP14 model applied to the COLOR-WARM simulation. For simplicity, when comparing results, we refer to COLOR + GP14 model results as COLOR, and COLOR-WARM + Re-GP14 results as COLOR-WARM.

3 GLOBAL GALAXY PROPERTIES IN THE TWO DARK MATTER MODELS

In this section, we compare the statistics of the galaxy populations in the two models, both in the local universe and at high redshift. We begin with a comparison of each model to observed stellar mass and luminosity functions in the local universe and the two point galaxy correlation function as a function of stellar mass. These statistics provide the most fundamental description of how galaxies populate

[1] This name was applied by Hellwing et al. (2016) to the simulation labelled 'DOVE' in Jenkins (2013), Sawala et al. (2015) and Fattahi et al. (2016).

[2] This model is available through the Millennium Data Base: http://virgodb.dur.ac.uk.

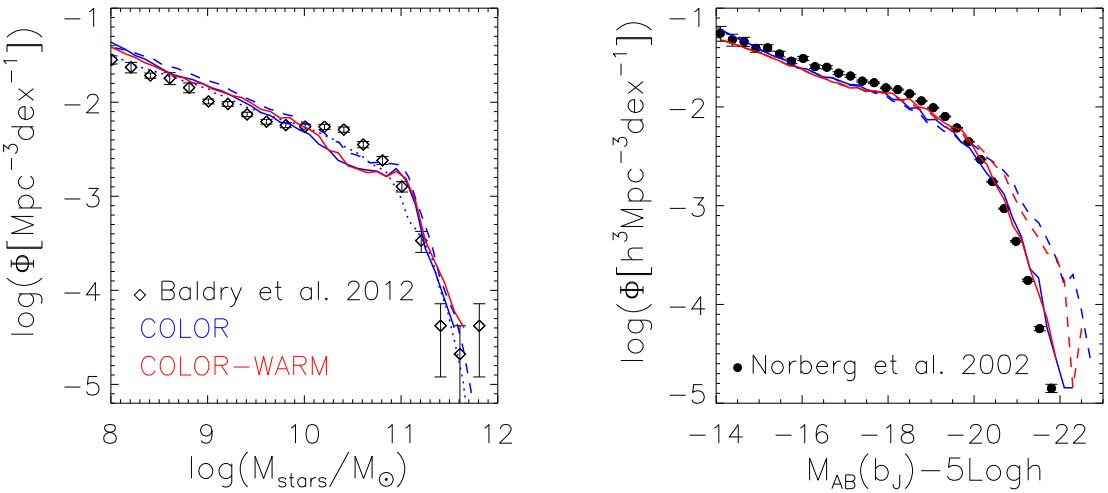

Figure 1. Left-hand panel: stellar mass functions of galaxies in the two models. Black symbols are the observations given by Baldry et al. (2012), corrected to a Kennicutt IMF (Lacey et al. 2016). The blue solid line is for the COLOR model, and the red solid line is for COLOR-WARM. The blue dashed line is the result of the GP14 model combined with MS-W7 simulation as shown in the GP14 paper. The blue dotted line shows the stellar mass function of the GP14 model combined with MS-W7 simulation obtained from the model broad-band photometry by SED fitting as given in the GP14 paper (see the text for more details). Right-hand panel: b_J band galaxy luminosity function in the two models. Solid lines are results including the attenuation by dust, while dashed lines are the ones without it. Black dots with error bars are 2dF results of Norberg et al. (2002).

dark matter haloes in each model. We then proceed to compare their stellar mass functions at high redshifts and the evolution of the star formation rate (SFR) density of the universe. Note that normally the plausible semi-analytic models are matched with observations at $z = 0$ and can be accepted within a larger variation than the errors of the observation data (Bower et al. 2010; Benson 2014; Rodrigues, Vernon & Bower 2017), and the two model results can be considered to be similar within that variation.

3.1 Present-day stellar mass and luminosity functions

The left-hand panel of Fig. 1 presents the $z = 0$ galaxy stellar mass functions of the CDM and WDM runs. The blue solid line corresponds to the COLOR result and the red solid line to the result of COLOR-WARM. As described in Section 2.2, we calibrate the stellar mass function of COLOR-WARM to reproduce that of COLOR at $z = 0$ over the stellar mass range $10^9 < M_{\rm stars}/(h^{-1}\,{\rm M}_\odot) < 10^{11}$. The right-hand panel of Fig. 1 shows the b_J-band luminosity function. The close correspondence between the $z = 0$ luminosity functions of COLOR-WARM and COLOR reflects the stellar mass function calibration.

In the left-hand panel of Fig. 1, the blue dashed line is the result of the GP14 model applied to the MS-W7 simulation. The difference between the blue solid and dashed lines is mainly due to cosmic variance (see Appendix B for further details). The blue dotted line in the same panel shows another version of this GP14 + MS-W7 mass function, in which the stellar masses are obtained by spectral energy distribution (SED) fitting, following an algorithm similar to that used in observations (Baldry et al. 2012; Mitchell et al. 2013; GP14). This reduces the inferred abundance at both low and high stellar masses, and smooths the bump near the 'knee' of the function. We show it here to emphasize that discrepancies between our baseline GP14 model and observations can be reduced when model stellar masses are obtained from SED fitting. This more complex calculation of the mass function is not used in the results we present here for COLOR and COLOR-WARM though, because our focus is on the difference between CDM and WDM models, rather than between either model and observations.

3.2 Galaxy correlation function

The two-point correlation function is a basic measure of the spatial clustering of galaxies. The dependence of galaxy clustering as a function of various intrinsic galaxy properties has been well determined by observations (e.g, Norberg et al. 2002; Li et al. 2006; Farrow et al. 2015; Shi et al. 2016). However, in galaxy formation models it is still difficult to reproduce the amplitude of correlation functions for low-mass galaxies and on small scales (Guo et al. 2011; Wang, Weinmann & Neistein 2012; Campbell et al. 2015).

In Fig. 2, we compare the projected galaxy correlation functions in different stellar mass bins from our simulated CDM and WDM galaxy populations. Due to the limited box size of the simulations, these correlation functions fall off more rapidly than the data at large scales (Orsi et al. 2008; Campbell et al. 2015). For the box size of our simulations, the correlation functions can be measured only up to scales of a few megaparsecs. The correlation functions of the CDM and WDM model variants are in good agreement for all stellar masses. Some difference is seen for the stellar mass bin $M_{\rm stars} = 10^{9.27\text{–}9.77}\,{\rm M}_\odot$, but with insufficient statistics to draw firm conclusions.

3.3 Stellar mass functions at high redshifts

Although the stellar mass functions of our GP14 and Re-GP14 models are almost identical by construction at $z = 0$, they are free to differ at higher redshifts. Such differences are expected from the different parameter choices that Re-GP14 requires to satisfy the observed constraint at $z = 0$. These parameter differences most likely reflect fundamental differences in how structure formation proceeds in CDM and WDM (Bode et al. 2001; Knebe et al. 2002; Angulo et al. 2013; Gao et al. 2015).

In Fig. 3, we plot stellar mass functions at four redshifts in both dark matter models. At $z < 3$, the stellar mass functions are quite similar. Towards higher redshift, however, massive galaxies are more abundant in COLOR-WARM than in COLOR. At $z = 6$, the difference is about three times at most, and at $z = 10$, the difference can be as high as nine times. This is consistent with the results

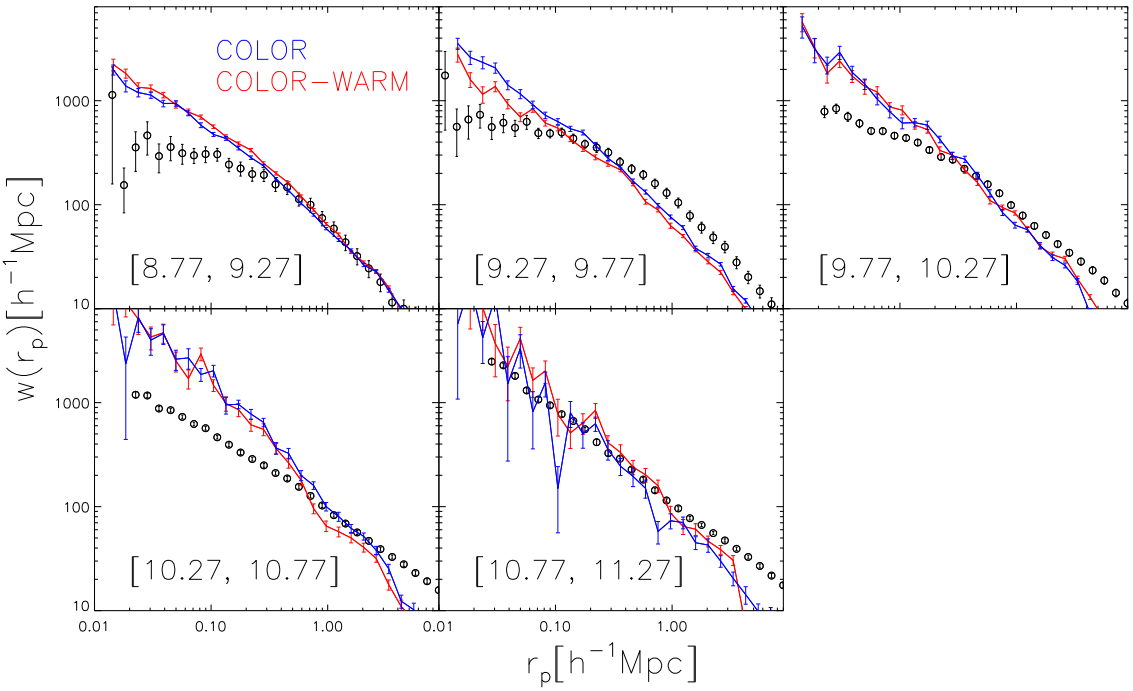

Figure 2. Projected two-point correlation functions of galaxies in the two models binned in stellar mass. Error bars are from bootstrapping simulation data (Barrow, Bhavsar & Sonoda 1984). The circles with error bars show the SDSS DR7 results (Li et al. 2006; Guo et al. 2011).

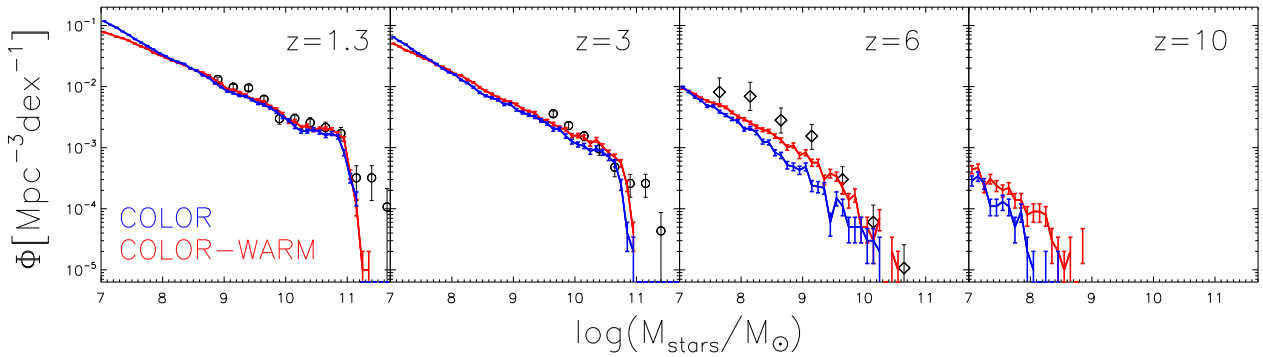

Figure 3. Galaxy stellar mass functions at redshifts of 1.3, 3, 6 and 10 in the two models. COLOR results are shown in blue and COLOR-WARM results in red, with Poisson error bars. Black circles with error bars in the two leftmost panels are the observational complete data results from Kajisawa et al. (2009) in redshift intervals of [1.0, 1.5] and [2.5, 3.5], respectively. Diamonds are observational data from González et al. (2011) at $<z> = 5.9$. Observed stellar masses are adjusted to the assumption of a Kennicutt IMF following Lacey et al. (2016).

of Bose et al. (2017), who found that, with the same semi-analytic model applied to a cold and a 3.3 keV WDM simulation, at redshifts greater than 5, the amplitude of the UV luminosity function in a WDM model was higher than that in a CDM model (although see also Dayal, Mesinger & Pacucci 2015, who do not find an excess of bright galaxies at high redshift in a 1.5 keV WDM model). Bose et al. (2017) attributed this to the fact that, in their models the brightest galaxies form through merger-triggered starbursts at high redshift, and this mechanism is more efficient in the WDM cosmology. We have checked that in our models, at $z > 3$, there are indeed more starburst galaxies in COLOR-WARM than in COLOR, consistent with this explanation.

3.4 Cosmic SFR densities

As discussed in the previous subsection, massive galaxies at high redshift form more efficiently in WDM models than in CDM models. This effect is also apparent in the evolution of the cosmic SFR density. In Fig. 4, the thick solid blue line shows the total SFR density in COLOR, and the thick solid red line its equivalent in COLOR-WARM. All galaxies with stellar mass more massive than $10^7\,M_\odot$ are included in the calculation. At $z < 3$, the total SFR densities in the two models differ by less than 0.07 dex. At higher redshift, the total SFR density in COLOR-WARM is larger than that in COLOR, up to ∼0.3 dex.

We also plot in Fig. 4 the contributions to the total SFR density made by galaxies in different ranges of stellar mass. At each redshift, we calculate the 85 per cent and 97 per cent distributions of galaxy stellar mass.[3] In Fig. 4, the contributions of the most

[3] At $z = 0$, the 85 per cent and 97 per cent distributions of galaxy stellar masses for COLOR are $10^{8.63}$ and $10^{9.84}\,M_\odot$, while those for COLOR-WARM are $10^{8.87}$ and $10^{10.01}\,M_\odot$.

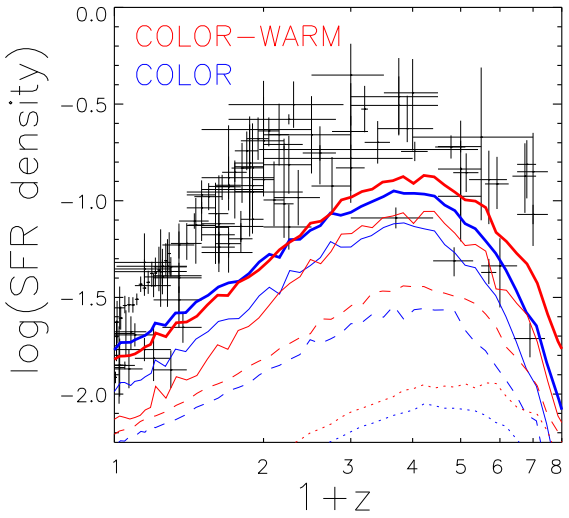

Figure 4. Cosmic star formation rate density $\rho_{\rm SFR}$ (in units of $h^2\,{\rm M}_\odot\,{\rm yr}^{-1}\,{\rm Mpc}^{-3}$) as a function of redshift in the models. COLOR results are shown as blue lines and COLOR-WARM results as red lines. Thick solid lines show the total SFR density. Thin lines with different line styles show the contributions to the total density from galaxies of different stellar mass ranges at the redshift of observation as follows. Thin solid: the top 3 per cent massive galaxies; dashed: galaxies with stellar mass between the 85 per cent and 97 per cent distributions; dotted: the 85 per cent least massive galaxies. As reference, black crosses are observational estimates compiled by Hopkins (2007), where SFRs have been adjusted to the assumption of a Kennicutt IMF following Lacey et al. (2016).

massive 3 per cent galaxies as a function of redshift are plotted in thin solid lines. Dashed lines give contributions of galaxies with stellar mass between the 85 per cent and 97 per cent distributions, and dotted lines are the contributions of the least massive 85 per cent galaxies. At all redshifts, the total SFR density is dominated by the most massive galaxy populations at the time. Comparing the two dark matter models, we see that for $z > 2$ the SFR densities of the most massive galaxies from COLOR-WARM are always higher than those in COLOR. The difference can be as high as 0.2 dex, corresponding to the difference in the total SFR density. This again reflects the more efficient formation of massive galaxies at redshifts $z > 2$ in the WDM model, consistent with the picture described in Section 3.3.

3.5 Mass assembly and SFR histories

We can use the galaxy merger trees associated with our models to trace the stellar mass and halo mass of $z = 0$ galaxies backwards in time. In Fig. 5, dashed lines show the mean halo mass growth history for the main progenitor[4] of central galaxies at $z = 0$, split into six logarithmic bins of $z = 0$ stellar mass bins (each of width 0.2 dex). Solid lines denote the corresponding mean growth histories of stellar mass. Dotted lines are the corresponding mean SFR histories. As in previous figures, COLOR results are shown by blue lines, and COLOR-WARM results by red lines.

Fig. 5 clearly shows that galaxies less massive than $10^{10}\,{\rm M}_\odot$ at $z = 0$ in COLOR-WARM assemble both their halo mass and stellar mass later than in COLOR, with lower SFR at high redshifts.

[4] We define the main progenitor by identifying the most bound 'core' of dark matter particles, rather than the most massive one, following the method of Jiang et al. (2014).

The differences between the two models are larger for lower mass galaxies. For galaxies with stellar mass of $10^{8.5}\,{\rm M}_\odot$ at $z = 0$, their mean stellar masses differ by more than 100 times at $z > 9$, and the mean halo masses differ by more than 30 times. For more massive galaxies, at a fixed stellar mass, halo mass grows at a similar rate in the two models but stellar mass assembles earlier (and SFR is correspondingly higher) at high redshift in COLOR-WARM. The difference in stellar mass is less than three times up to $z = 10$.

For galaxies in the range $10^{10} < M_\star < 10^{10.5}\,{\rm M}_\odot$, at very high redshift ($z > 9$) there is a trend such that stellar masses in the WDM model are lower than those in the CDM model. This is due to the later formation of the earliest progenitors in the WDM model. At redshifts lower than ∼9, galaxies in the WDM model catch up through more gas-rich mergers and have higher stellar mass in WDM than in CDM. These differences are consistent with those reported by Bose et al. (2017), who used initial power spectrum corresponding to 3.3 keV thermal relic mass particle.

4 GALAXY POPULATIONS IN VOIDS AND IN THE LOCAL VOLUME

Numerical simulations of structure formation indicate that the differences between WDM and CDM models are most pronounced on small scales and in underdense regions (e.g. Bode et al. 2001; Knebe et al. 2002, 2003; Angulo et al. 2013). Anticipating that these differences may in turn influence the properties of galaxies in such regions, we explore voids in the distribution of galaxies, and analogues of the Local Volume and the Local Void in our models. In the nearby Universe, galaxy counts are roughly 80 per cent complete down to a faint limit of $m_B = 17.5$ (Karachentsev, Kaisina & Makarov 2014), which makes it possible to compare faint galaxies with the observational data in order to constrain the identity of dark matter.

4.1 Galaxy population in voids

Voids in the distribution of galaxies have been noticed for several decades (e.g. Jõeveer, Einasto & Tago 1978; Tully 1988; Peebles 2001), and are large, underdense regions in the Universe. Many algorithms define voids as underdense spheres (e.g. Kauffmann & Fairall 1991; Müller et al. 2000; Colberg et al. 2008). More sophisticated algorithms find voids without making any assumption about their shape (e.g. Platen, van de Weygaert & Jones 2007; Neyrinck 2008). In the Local Universe, typical sizes of voids in the galaxy distribution vary from around 6 Mpc to more than 20 Mpc, in a galaxy survey like SDSS (e.g. Ceccarelli et al. 2013). Voids in WDM cosmology have been investigated in the recent works of Reed et al. (2015), who studied galaxy clustering and void volume fraction, and Yang et al. (2015), who measured the statistics and density profiles of voids in CDM cosmology and three WDM cosmologies with $m_x = 1.4$, 0.8 and 0.4 keV.

For our purposes, we define voids in our $z = 0$ galaxy catalogue as underdense spheres of a fixed radius $10^{-1}\,h$ Mpc; we choose this value because it is a typical scale of voids probed by galaxy redshift surveys (Ceccarelli et al. 2013). We have checked that when choosing an alternative radius of $5^{-1}\,h$ Mpc or $15^{-1}\,h$ Mpc, the results shown below remain similar. For each of our simulations, we first choose 10 000 random points in the whole simulation box as the centres of spheres. We then compute the galaxy number density in each sphere. All galaxies of stellar mass $>10^7\,h^{-1}\,{\rm M}_\odot$ are considered. Galaxies with this lower limit stellar mass are typically hosted by haloes with masses of $10^{10-10.5}\,h^{-1}\,{\rm M}_\odot$ (see the stellar

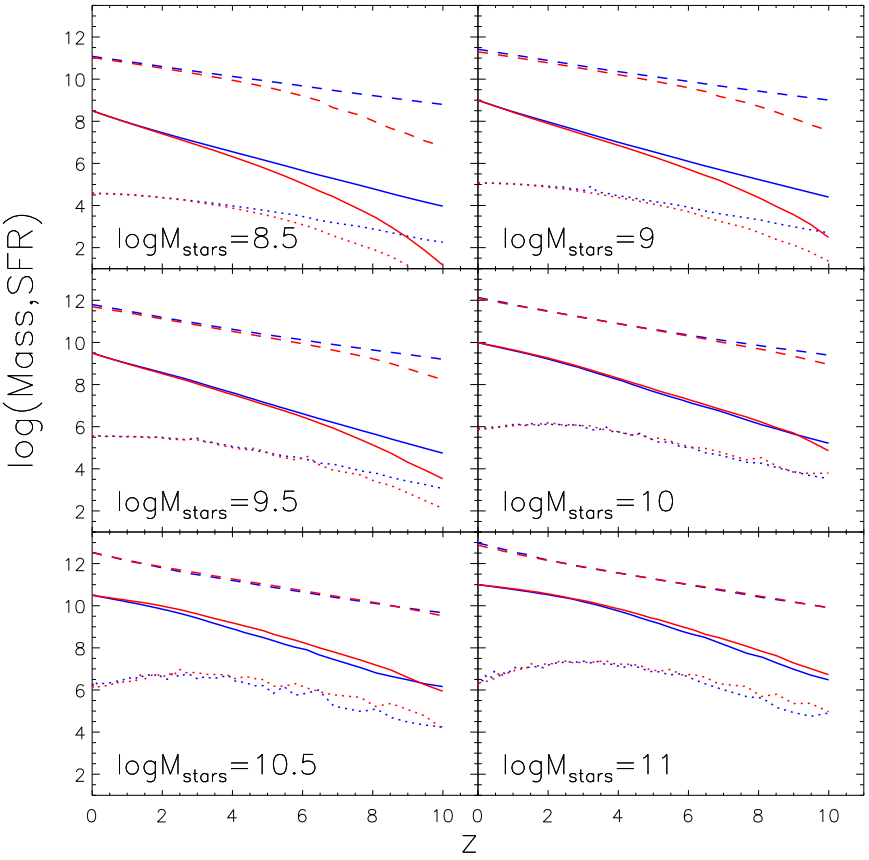

Figure 5. Mean stellar mass (solid lines) and halo mass (dashed lines) assembly histories of central galaxies as a function of redshift at six stellar masses at $z = 0$ (with bin width 0.2 in logarithm). Masses are in units of solar mass. Dotted lines show the SFR histories of these galaxies, in unit of $h^{-1}\,\mathrm{M}_{\odot}\,\mathrm{Gyr}^{-1}$. For clarity, dotted lines are moved downward by 3 dex. Blue lines show COLOR results and red lines are from COLOR-WARM.

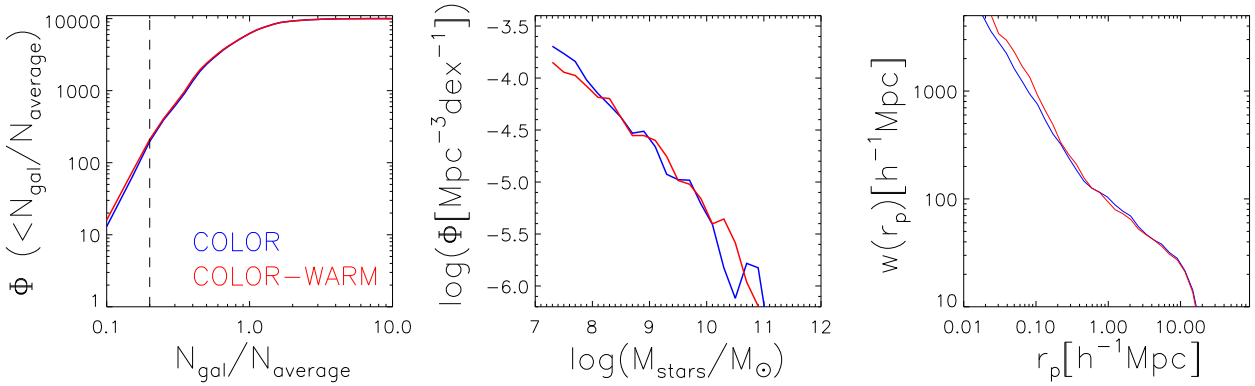

Figure 6. Left-hand panel: cumulative number counts of spheres of radius $10\,h^{-1}$ Mpc, as a function of the ratio between galaxy number in the sphere and the average galaxy number in a sphere of the same radius. We define voids as those spheres with ratios smaller than 0.2 (Neyrinck 2008); this criterion is shown by the vertical dashed line. Middle panel: mean stellar mass function of galaxies in voids. Right-hand panel: two point projected correlation functions of void galaxies.

mass–halo mass relation in Fig. C2). Such haloes contain $\gtrsim$1000 particles and are therefore well above the resolution limit of the simulations.

In the left-hand panel of Fig. 6, we show the cumulative number counts of these randomly placed spheres as a function of the ratio between the number of galaxies in the sphere and N_{average}, the average number of galaxies in a sphere of the same volume over the whole simulation box. $N_{\mathrm{average}} = 246$ for COLOR, and for COLOR-WARM $N_{\mathrm{average}} = 202$. We define a sphere as a void when the number of galaxies included in the sphere is less than 20 per cent of the average, which number is often used by the previous works studying properties of voids (e.g. Neyrinck 2008). This criterion is shown as a vertical dashed line in the left-hand panel of the figure. By this definition, there are 211 voids in the COLOR-WARM simulation, which is close to the 197 voids identified in COLOR.

We refer to galaxies that reside in voids as void galaxies. The middle and right-hand panels of Fig. 6 present the properties of void galaxies in the two models. The middle panel shows the

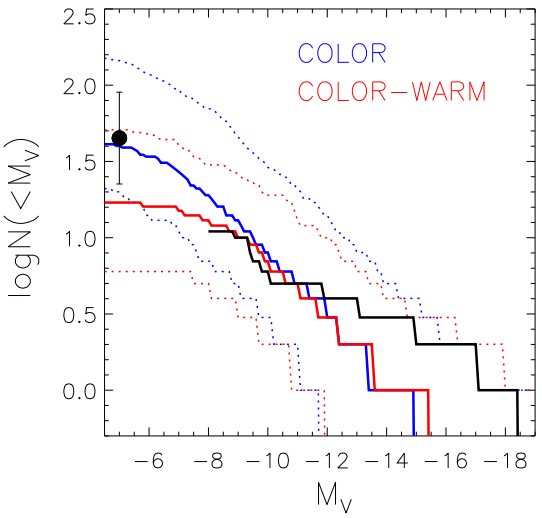

Figure 7. Cumulative luminosity function for MW-analogues satellite galaxies. Solid colour curves show the median value and dotted colour curves give 10 and 90 per cent distributions of the results in the two models. The black line shows the result for the 11 classical satellites of the Milky Way, and the black dot is the estimation of Koposov et al. (2008), while the error bar is assigned to be a factor of 2 to account for the large intrinsic uncertainty.

average stellar mass function of void galaxies, which is broadly similar in the two models. The right-hand panel of Fig. 6 shows the two-point projected correlation function of void galaxies. The results are again similar in the two models. Our finding is consistent with the recent work of Reed et al. (2015), who compared galaxy clustering and void (defined as spheres containing zero galaxies) volume fraction between WDM and CDM cosmologies, and found almost no difference between the two.

4.2 Galaxy abundance in the Milky Way and the Local Volume

4.2.1 The abundance of Milky Way satellites

The CDM cosmogony gives rise to many more substructures in haloes of mass comparable to that of the Milky Way and M31 than there are known satellites of those two galaxies (Klypin et al. 1999; Moore et al. 1999; Stadel et al. 2009). This discrepancy is known as the missing satellite problem. The widely accepted solution to this problem is that some substructures fail to host enough star formation due to baryonic effects and/or reionization (e.g. Kauffmann, White & Guiderdoni 1993; Benson et al. 2002; Li, De Lucia & Helmi 2010; Governato et al. 2015; Sawala et al. 2015, 2016). Recent semi-analytic models combined with high-resolution simulations predict satellite counts consistent with recent observations in both the CDM cosmology (e.g. Guo et al. 2011, 2015) and a WDM cosmology with $m_x = 3.3$ keV (Bose et al. 2017).

Following Guo et al. (2011), we select Milky Way-like galaxies to be disc-dominated central galaxies with bulge-to-total mass ratio greater than 0.5, and with a stellar mass between 4×10^{10} and $8 \times 10^{10}\,\mathrm{M}_{\odot}$. 120 MW-analogues are selected in COLOR and 68 MW-analogues are selected in COLOR-WARM. Satellites of each MW-analogue are defined as all galaxies within a sphere of radius 280 kpc of the central galaxy. Fig. 7 presents the cumulative luminosity function for MW-analogue satellite galaxies in our two models. The black line gives the result for the 11 classical satellites of the Milky Way, and the black dot is the estimation of Koposov et al. (2008), which is based on the estimate of 45 MW satellites with $M_V < -5$ and $r < 280$ kpc from SDSS DR5. Recently, more satellites of MW have been discovered by the Dark Energy Survey (DES; Bechtol et al. 2015; Drlica-Wagner et al. 2015; Koposov et al. 2015), the VST-Atlas (Torrealba et al. 2016) and Pan-STARRS 3π surveys (Laevens et al. 2015a,b). Fig. 11 of Bose et al. (2017) has included these latest observed satellites, which is consistent with the data shown in our Fig. 7, with more data points and extending to fainter luminosity. However, the newly found MW satellites have anisotropic distribution, and the completeness is quite uncertain (for detail discussion, see Lovell et al. 2016). We therefore choose to show here the more conservative observational data as reference.

In Fig. 7, regions between dotted lines indicate the 10th and 90th percentile distribution of the two model results, and both cover the observation. The results from the two models are quite similar for magnitudes M_V brighter than -10. At fainter magnitudes, MW-analogues in COLOR host more satellites than those in COLOR-WARM. The difference in the median becomes apparent for satellites with absolute magnitude fainter than -8. At $M_V = -6$, the difference in the median is as large as 0.4 dex. The difference between CDM and WDM cosmologies in our models is larger than that found in Bose et al. (2017, fig. 10). This is mainly due to the fact that the WDM particle we adopt has a longer free-streaming length than the 3.3 keV particle used in their paper, which greatly reduces the number of low-mass dark matter haloes. Other than that, effects caused by different simulations used like cosmic variance may also play a role.

4.2.2 The Local Void

Full sky galaxy surveys in the local Universe have revealed that about a third of the Local Volume contains only three galaxies (Peebles 2001; Peebles & Nusser 2010). As noted above, these surveys are about 80 per cent complete to $m_B = 17.5$ (Karachentsev et al. 2014). The emptiness of this region, known as Local Void, has been claimed as a potential challenge to the standard ΛCDM cosmogony (Peebles & Nusser 2010). Xie, Gao & Guo (2014) studied the probability of finding a region like the Local Void in a simulated ΛCDM galaxy catalogue. They found a probability as high as 14 per cent, which suggests that the emptiness of the Local Void may not be in conflict with ΛCDM. As the Local Volume containing the Local Void provides a laboratory for observing the faintest galaxies in the Universe, we study statistics of 'Local Volumes' and 'Local Voids' in both our WDM and CDM catalogues to investigate if any differences can be measured.

Following the method and definitions of Xie et al. (2014), 'Local Volumes' in the simulations are defined as regions within a radial range of [1,8 Mpc] around simulated MW-analogues, which are selected to be central disc galaxies with bulge-to-total stellar mass ratio less than 0.5, and with B-band magnitude within the range $[-21.5, -19.5]$.[5] Since our MW and M31 are separated by a distance of 0.77 Mpc, 'Local Volumes' are further selected to have a companion giant galaxy with a stellar mass similar to that of the M31, with stellar mass in the range $[0.5 \times M_{\mathrm{MW}}, 2 \times M_{\mathrm{MW}}]$, within

[5] Here, we choose the criterion of B-band magnitude rather than stellar mass to select MW-like galaxies, to get more simulated 'Local Volumes' for statistical study. There are too few 'Local Volumes' if MW-analogues are selected by stellar mass, due to the lack of M* galaxies in the stellar mass functions in our models as shown in Fig. 1.

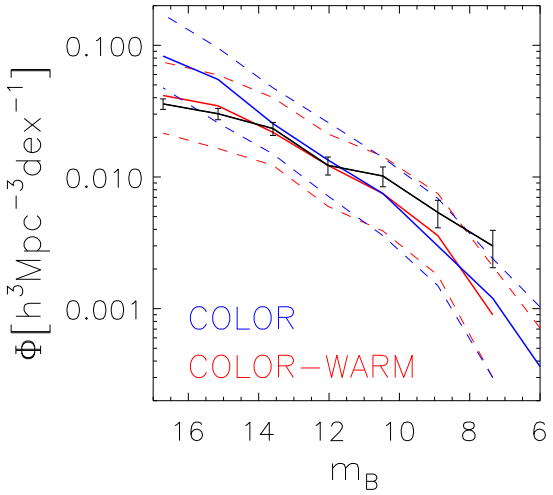

Figure 8. The apparent *B*-band magnitude luminosity function of galaxies in simulated Local Volumes. The observed luminosity function calculated based on the data provided by Karachentsev et al. (2014) is shown as a black line. Simulated Local Volumes are shown by red (COLOR-WARM) and blue (COLOR) lines, with solid lines showing the median value and dashed lines show the 68 percentile envelope of the distribution.

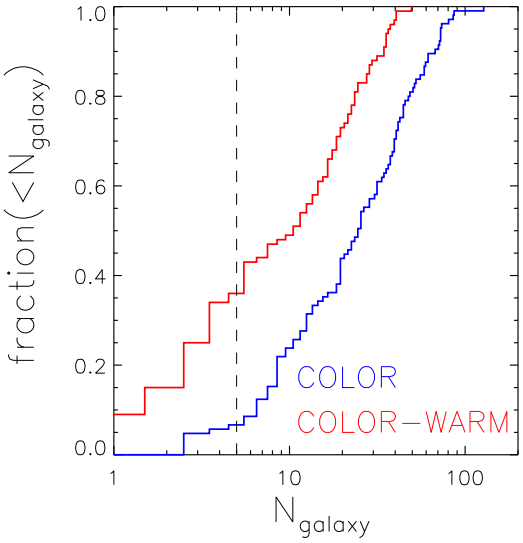

Figure 9. The cumulative fraction of simulated Local Void samples as a function of the number of galaxies enclosed in the void. The vertical dashed line indicates the number of five galaxies observed in the real Local Void.

1 Mpc from the 'Milky Way'.[6] In addition, systems with clusters (haloes more massive than $10^{14}\,M_\odot$) close by (<10 Mpc) are excluded, to mimic the relative isolated environment of the Milky Way, where the Virgo cluster is about 16.5 Mpc away (Mei et al. 2007). We thus determine that there are 105 thus-defined Local Volumes in COLOR and 100 in COLOR-WARM.

Fig. 8 presents a comparison of the luminosity functions of galaxies in the simulated 'Local Volumes'. As reference, black line with error bars gives the observed luminosity function based on the data provided by Karachentsev et al. (2014), including all galaxies within 1–8 Mpc to be consistent with the simulated 'Local Volumes'. Note that the completeness of the observed galaxies should be different at different magnitudes, with brighter galaxies being more completely observed. However, the completeness is still uncertain in observation and therefore not corrected for the observation result shown.

Fig. 8 shows that the bright end of the luminosity function in the two models are similar. Observation at the bright end is higher than the median values of both models. At the faint end, COLOR-WARM produces lower amplitude up to a factor of 2, and thus achieves a better match to the observation than does COLOR. Apart from the luminosity function of galaxies in the Local Volume, Klypin et al. (2015) and Schneider et al. (2016) studied the H I velocity function of galaxies in the Local Volume in both CDM and WDM models. Schneider et al. (2016) found that the discrepancy between observation and CDM model disappears in warm and mixed (warm plus cold) dark matter models.

Note that galaxies shown in Fig. 8 can have stellar masses as low as around $10^6\,M_\odot$, while for the stellar mass functions shown in Fig. 1, only galaxies more massive than $10^8\,M_\odot$ are presented, and in Fig. 6, galaxies more massive than $10^7\,M_\odot$ are included. If we also plot the stellar mass function (SMF) down to $10^6\,M_\odot$, there are more galaxies in the COLOR box as a whole as well (see Fig. C1), which is not in conflict with the results seen here. On the other hand, Fig. C1 indicates that SMFs become shallower below a few times $10^6\,M_\odot$, which marks the resolution limit of the two models. Therefore, results shown in Fig. 8 are not quite complete. However, with the trend that the two models have larger difference towards lower masses, the results in Fig. 8 should remain similar if a higher resolution simulation is used.

For our next step, we follow Xie et al. (2014) in identifying simulated 'Local Voids' as the most empty, truncated, cone-shaped region with a solid angle π. Fig. 9 shows the cumulative fraction of the simulated 'Local Voids' as a function of the number of galaxies enclosed in the void. Simulated 'Local Voids' in COLOR-WARM are overall emptier than the ones in COLOR. The observed Local Void around the real Milky Way contains fewer than five galaxies (when Poisson noise is taken into account), indicated by the vertical dashed line in Fig. 9. Statistically, 5.7 per cent of simulated Local Voids are as empty as the observed Local Void in COLOR.[7] The number of such voids in COLOR-WARM is much higher, up to approximately 34 per cent. Therefore, in our models the probability of hosting the Local Void is more than five times higher in this WDM model than in the CDM cosmology.

5 CONCLUSION AND DISCUSSIONS

This work explores how properties of the galaxy population change under different assumptions about the mass of dark matter particles, going from a CDM to a WDM cosmogony. We have chosen a WDM particle with a linear power-spectrum consistent with a 1.5 keV thermal relic, which is warmer than the latest Ly α forest constraint allows, to maximize the differences that arise. The two simulations we use, COLOR and COLOR-WARM, have sufficient resolution and volume to explore this problem with unprecedented statistics and precision.

[6] We have checked that our conclusion in this subsection will not be affected if this distance of 1 Mpc is changed to 2 Mpc.

[7] Note that this probability is somewhat different from the 14 per cent result given by Xie et al. (2014). The difference is expected because of the different simulations used, the different galaxy formation models applied, and also due to cosmic variance.

We combine the two simulations with the GALFORM semi-analytic model of galaxy formation and evolution. We apply the GALFORM model of GP14 in our CDM simulation. In our WDM simulation, we retune the parameters of this model to bring the galaxy stellar mass function at $z = 0$ into agreement with that of the CDM simulation in the mass range $10^9 < M_{\rm stars}/(h^{-1}\,{\rm M}_\odot) < 10^{11}$.

We have compared various properties of the model galaxy population to $z = 10$. Many of the properties we examine are indistinguishable between the two dark matter models, including the spatial clustering of galaxies (Fig. 2), and the statistics of the galaxy population in underdense regions (Fig. 6). However, differences become more obvious at higher redshifts, with massive galaxies forming more efficiently in the WDM model. This is indicated by results showing that the high-mass end of the stellar mass functions in the WDM model are up to about 3 and 9 times higher than in CDM at $z = 6$ and 10, respectively (Fig. 3). Moreover, at $z > 3$, the SFR density in the WDM model is up to two times higher (Fig. 4). At $z = 0$, a transition is evident at stellar mass of around $10^{10}\,{\rm M}_\odot$ (Fig. 5). Galaxies less massive than $10^{10}\,{\rm M}_\odot$ assemble both stellar mass and halo mass later in WDM compared to a CDM cosmology. The difference is greatest for low-mass galaxies (stellar mass $10^{8.5}\,{\rm M}_\odot$), which is more than 100 times for the mean stellar mass and more than 30 times for the mean halo mass at $z > 9$. Galaxies more massive than $10^{10}\,{\rm M}_\odot$ assemble their stellar masses somewhat earlier in the WDM model, with differences in stellar mass up to a factor of 3 for redshifts between $\sim$3 and 10. The difference between CDM and WDM models at $z > 7$ is also seen in Bose et al. (2017), with a rest mass of 3.3 keV in WDM model adopted, but the difference is indistinguishable by current observation.

In the local universe, the most pronounced differences between the two dark matter models are found in the counts of galaxies in analogues of the Local Volume and the probability of observing a region as empty as the Local Void (Section 4.2.2). The simulated 'Local Volumes' have lower number density by up to a factor of 2 at the faint end of the luminosity function in the WDM model (Fig. 8). The probability of a region as empty as the observed Local Void is as high as 34 per cent in the WDM model, five times higher than that in the CDM model (Fig. 9). A more complete Local Volume galaxy census (e.g. the Dark Energy Spectroscopic Instrument's Bright Galaxy Survey; DESI Collaboration 2016) should therefore provide a way to constrain the nature of dark matter.

ACKNOWLEDGEMENTS

We acknowledge Ran Li, Hong Guo for the helpful discussions. LW acknowledges support from the NSFC grants programme (no. 11573031, no. 11133003). VGP acknowledges past support from the European Research Council Starting Grant (DEGAS-259586). WAH is supported by the European Research Council grant through 646702 (CosTesGrav) and the Polish National Science Center under contract #UMO-2012/07/D/ST9/02785.

The work was carried out at National Supercomputer Center in Tianjin, and the calculations were performed on TianHe-1A.

This work used the DiRAC Data Centric system at Durham University, operated by the Institute for Computational Cosmology on behalf of the STFC DiRAC HPC Facility (www.dirac.ac.uk). This equipment was funded by BIS National E-infrastructure capital grant ST/K00042X/1, STFC capital grants ST/H008519/1 and ST/K00087X/1, STFC DiRAC Operations grant ST/K003267/1 and Durham University. DiRAC is part of the National E-Infrastructure.

This work is part of the D-ITP consortium, a programme of the Netherlands Organization for Scientific Research (NWO) that is funded by the Dutch Ministry of Education, Culture and Science (OCW).

REFERENCES

Ackermann M. et al., 2015, Phys. Rev. Lett., 115, 231301
Akerib D. S. et al., 2014, Phys. Rev. Lett., 112, 091303
Angulo R. E., Hahn O., Abel T., 2013, MNRAS, 434, 3337
Baldry I. K. et al., 2012, MNRAS, 421, 621
Barrow J. D., Bhavsar S. P., Sonoda D. H., 1984, MNRAS, 210, 19P
Bechtol K. et al., 2015, ApJ, 807, 50
Benson A. J., 2014, MNRAS, 444, 2599
Benson A. J., Frenk C. S., Lacey C. G., Baugh C. M., Cole S., 2002, MNRAS, 333, 177
Benson A. J. et al., 2013, MNRAS, 428, 1774
Bertone G., Hooper D., 2016, preprint (arXiv:1605.04909)
Bode P., Ostriker J. P., Turok N., 2001, ApJ, 556, 93
Bose S., Hellwing W. A., Frenk C. S., Jenkins A., Lovell M. R., Helly J. C., Li B., 2016, MNRAS, 455, 318
Bose S. et al., 2017, MNRAS, 464, 4520
Bower R. G., Benson A. J., Malbon R., Helly J. C., Frenk C. S., Baugh C. M., Cole S., Lacey C. G., 2006, MNRAS, 370, 645
Bower R. G., Vernon I., Goldstein M., Benson A. J., Lacey C. G., Baugh C. M., Cole S., Frenk C. S., 2010, MNRAS, 407, 2017
Boylan-Kolchin M., Bullock J. S., Kaplinghat M., 2012, MNRAS, 422, 1203
Busha M. T., Evrard A. E., Adams F. C., 2007, ApJ, 665, 1
Campbell D. J. R. et al., 2015, MNRAS, 452, 852
Ceccarelli L., Paz D., Lares M., Padilla N., Lambas D. G., 2013, MNRAS, 434, 1435
Colberg J. M. et al., 2008, MNRAS, 387, 933
Cole S., Lacey C. G., Baugh C. M., Frenk C. S., 2000, MNRAS, 319, 168
Colín P., Valenzuela O., Avila-Reese V., 2008, ApJ, 673, 203
Colín P., Avila-Reese V., González-Samaniego A., Velázquez H., 2015, ApJ, 803, 28
Davis M., Efstathiou G., Frenk C. S., White S. D. M., 1985, ApJ, 292, 371
Dayal P., Mesinger A., Pacucci F., 2015, ApJ, 806, 67
de Souza R. S., Mesinger A., Ferrara A., Haiman Z., Perna R., Yoshida N., 2013, MNRAS, 432, 3218
Del Popolo A., Pace F., 2016, Ap&SS, 361, 162
DESI Collaboration, 2016, preprint (arXiv:1611.00036)
Destri C., de Vega H. J., Sanchez N. G., 2013, Phys. Rev. D, 88, 083512
Drlica-Wagner A. et al., 2015, ApJ, 813, 109
Farrow D. J. et al., 2015, MNRAS, 454, 2120
Fattahi A. et al., 2016, MNRAS, 457, 844
Frenk C. S., White S. D. M., 2012, Ann. Phys., Lpz., 524, 507
Gao L., Theuns T., 2007, Science, 317, 1527
Gao L., Theuns T., Springel V., 2015, MNRAS, 450, 45
Garzilli A., Boyarsky A., Ruchayskiy O., 2015, preprint (arXiv:1510.07006)
Gilmore G., Wilkinson M. I., Wyse R. F. G., Kleyna J. T., Koch A., Evans N. W., Grebel E. K., 2007, ApJ, 663, 948
González V., Labbé I., Bouwens R. J., Illingworth G., Franx M., Kriek M., 2011, ApJ, 735, L34
Gonzalez-Perez V., Lacey C. G., Baugh C. M., Lagos C. D. P., Helly J., Campbell D. J. R., Mitchell P. D., 2014, MNRAS, 439, 264 (GP14)
González-Samaniego A., Avila-Reese V., Colín P., 2016, ApJ, 819, 101
Governato F. et al., 2015, MNRAS, 448, 792
Guo Q. et al., 2011, MNRAS, 413, 101
Guo Q., White S., Angulo R. E., Henriques B., Lemson G., Boylan-Kolchin M., Thomas P., Short C., 2013, MNRAS, 428, 1351
Guo Q., Cooper A. P., Frenk C., Helly J., Hellwing W. A., 2015, MNRAS, 454, 550
Hellwing W. A., Frenk C. S., Cautun M., Bose S., Helly J., Jenkins A., Sawala T., Cytowski M., 2016, MNRAS, 457, 3492
Herpich J., Stinson G. S., Macciò A. V., Brook C., Wadsley J., Couchman H. M. P., Quinn T., 2014, MNRAS, 437, 293
Hopkins A. M., 2007, in Afonso J., Ferguson H. C., Mobasher B., Norris R., eds, ASP Conf. Ser. Vol. 380. At the Edge of the Universe: Latest

Results from the Deepest Astronomical Surveys. Astron. Soc. Pac., San Francisco, p. 423
Jenkins A., 2013, MNRAS, 434, 2094
Jiang L., Helly J. C., Cole S., Frenk C. S., 2014, MNRAS, 440, 2115
Jõeveer M., Einasto J., Tago E., 1978, MNRAS, 185, 357
Kajisawa M. et al., 2009, ApJ, 702, 1393
Kamada A., Yoshida N., Kohri K., Takahashi T., 2013, J. Cosmol. Astropart. Phys., 3, 8
Kang X., Macciò A. V., Dutton A. A., 2013, ApJ, 767, 22
Karachentsev I. D., Kaisina E. I., Makarov D. I., 2014, AJ, 147, 13
Kauffmann G., Fairall A. P., 1991, MNRAS, 248, 313
Kauffmann G., White S. D. M., Guiderdoni B., 1993, MNRAS, 264, 201
Klypin A., Kravtsov A. V., Valenzuela O., Prada F., 1999, ApJ, 522, 82
Klypin A., Karachentsev I., Makarov D., Nasonova O., 2015, MNRAS, 454, 1798
Knebe A., Devriendt J. E. G., Mahmood A., Silk J., 2002, MNRAS, 329, 813
Knebe A., Devriendt J. E. G., Gibson B. K., Silk J., 2003, MNRAS, 345, 1285
Komatsu E. et al., 2011, ApJS, 192, 18
Koposov S. et al., 2008, ApJ, 686, 279
Koposov S. E., Belokurov V., Torrealba G., Evans N. W., 2015, ApJ, 805, 130
Lacey C. G. et al., 2016, MNRAS, 462, 3854
Laevens B. P. M. et al., 2015a, ApJ, 802, L18
Laevens B. P. M. et al., 2015b, ApJ, 813, 44
Lagos C. d. P., Bayet E., Baugh C. M., Lacey C. G., Bell T. A., Fanidakis N., Geach J. E., 2012, MNRAS, 426, 2142
Lagos C. d. P., Padilla N. D., Davis T. A., Lacey C. G., Baugh C. M., Gonzalez-Perez V., Zwaan M. A., Contreras S., 2015, MNRAS, 448, 1271
Lee J. et al., 2014, MNRAS, 445, 4197
Li C., Kauffmann G., Jing Y. P., White S. D. M., Börner G., Cheng F. Z., 2006, MNRAS, 368, 21
Li Y.-S., De Lucia G., Helmi A., 2010, MNRAS, 401, 2036
Li R., Frenk C. S., Cole S., Gao L., Bose S., Hellwing W. A., 2016, MNRAS, 460, 363
Li R., Frenk C. S., Cole S., Wang Q., Gao L., 2017, MNRAS, 468, 1426
Lovell M. R. et al., 2012, MNRAS, 420, 2318
Lovell M. R., Frenk C. S., Eke V. R., Jenkins A., Gao L., Theuns T., 2014, MNRAS, 439, 300
Lovell M. R. et al., 2016, MNRAS, 461, 60
Lovell M. R., Gonzalez-Perez V., Bose S., Boyarsky A., Cole S., Frenk C. S., Ruchayskiy O., 2016b, preprint (arXiv:1611.00005)
Lovell M. R. et al., 2016c, preprint (arXiv:1611.00010)
Ludlow A. D., Bose S., Angulo R. E., Wang L., Hellwing W. A., Navarro J. F., Cole S., Frenk C. S., 2016, MNRAS, 460, 1214
Macciò A. V., Paduroiu S., Anderhalden D., Schneider A., Moore B., 2013, MNRAS, 428, 3715
Maio U., Viel M., 2015, MNRAS, 446, 2760
Mei S. et al., 2007, ApJ, 655, 144
Menci N., Fiore F., Lamastra A., 2012, MNRAS, 421, 2384
Menci N., Fiore F., Lamastra A., 2013, ApJ, 766, 110
Merson A. I., Baugh C. M., Gonzalez-Perez V., Abdalla F. B., Lagos C. d. P., Mei S., 2016, MNRAS, 456, 1681
Mitchell P. D., Lacey C. G., Baugh C. M., Cole S., 2013, MNRAS, 435, 87
Moore B., Quinn T., Governato F., Stadel J., Lake G., 1999, MNRAS, 310, 1147
Müller V., Arbabi-Bidgoli S., Einasto J., Tucker D., 2000, MNRAS, 318, 280
Navarro J. F., Eke V. R., Frenk C. S., 1996, MNRAS, 283, L72
Neyrinck M. C., 2008, MNRAS, 386, 2101
Nierenberg A. M., Treu T., Menci N., Lu Y., Wang W., 2013, ApJ, 772, 146
Norberg P. et al., 2002, MNRAS, 332, 827
Orsi A., Lacey C. G., Baugh C. M., Infante L., 2008, MNRAS, 391, 1589
Pacucci F., Mesinger A., Haiman Z., 2013, MNRAS, 435, L53
Peebles P. J. E., 2001, ApJ, 557, 495
Peebles P. J. E., Nusser A., 2010, Nature, 465, 565
Planck Collaboration XI, 2016, A&A, 594, A11
Platen E., van de Weygaert R., Jones B. J. T., 2007, MNRAS, 380, 551
Polisensky E., Ricotti M., 2010, BAAS, 42, 232
Power C., Robotham A. S. G., 2016, ApJ, 825, 31
Reed D. S., Schneider A., Smith R. E., Potter D., Stadel J., Moore B., 2015, MNRAS, 451, 4413
Rodrigues L. F. S., Vernon I., Bower R. G., 2017, MNRAS, 466, 2418
Sánchez A. G. et al., 2017, MNRAS, 464, 1640
Sawala T. et al., 2015, MNRAS, 448, 2941
Sawala T. et al., 2016, MNRAS, 456, 85
Schneider A., Smith R. E., Macciò A. V., Moore B., 2012, MNRAS, 424, 684
Schneider A., Trujillo-Gomez S., Papastergis E., Reed D. S., Lake G., 2016, preprint (arXiv:1611.09362)
Seljak U., Zaldarriaga M., 1996, ApJ, 469, 437
Shao S., Gao L., Theuns T., Frenk C. S., 2013, MNRAS, 430, 2346
Shi F. et al., 2016, ApJ, 833, 241
Smith R. E., Markovic K., 2011, Phys. Rev. D, 84, 063507
Springel V., 2005, MNRAS, 364, 1105
Springel V., White S. D. M., Tormen G., Kauffmann G., 2001, MNRAS, 328, 726
Springel V. et al., 2008, MNRAS, 391, 1685
Stadel J., Potter D., Moore B., Diemand J., Madau P., Zemp M., Kuhlen M., Quilis V., 2009, MNRAS, 398, L21
Torrealba G. et al., 2016, MNRAS, 463, 712
Tremaine S., Gunn J. E., 1979, Phys. Rev. Lett., 42, 407
Tully R. B., 1988, Nearby Galaxies Catalog. Cambridge Univ. Press, Cambridge
Viel M., Lesgourgues J., Haehnelt M. G., Matarrese S., Riotto A., 2005, Phys. Rev. D, 71, 063534
Viel M., Becker G. D., Bolton J. S., Haehnelt M. G., 2013, Phys. Rev. D, 88, 043502
Vogelsberger M., Zavala J., Loeb A., 2012, MNRAS, 423, 3740
Walker M. G., Peñarrubia J., 2011, ApJ, 742, 20
Wang J., White S. D. M., 2007, MNRAS, 380, 93
Wang L., Weinmann S. M., Neistein E., 2012, MNRAS, 421, 3450
Watson C. R., Li Z., Polley N. K., 2012, J. Cosmol. Astropart. Phys., 3, 18
Xie L., Gao L., Guo Q., 2014, MNRAS, 441, 933
Yang L. F., Neyrinck M. C., Aragón-Calvo M. A., Falck B., Silk J., 2015, MNRAS, 451, 3606
Zavala J., Jing Y. P., Faltenbacher A., Yepes G., Hoffman Y., Gottlöber S., Catinella B., 2009, ApJ, 700, 1779
Zavala J., Vogelsberger M., Walker M. G., 2013, MNRAS, 431, L20

APPENDIX A: HALO MASS FUNCTIONS IN SIMULATIONS

Fig. A1 shows the FOF halo mass functions at different redshifts in the COLOR and COLOR-WARM simulations as described in Section 2.1. WDM halo mass functions flatten towards the low-mass end compared to those in CDM. As first indicated by Wang & White (2007), spurious haloes form due to a numerical discreetness effect in warm and hot dark matter simulations. The mass limit of dark matter haloes below which spurious haloes form depends on the N-body particle mass of the simulation and the WDM particle mass assumed. In COLOR-WARM, the N-body mass resolution is $m_{\rm dm} = 6.20 \times 10^6\, h^{-1}\,{\rm M}_\odot$, and the WDM particle mass is $m_x = 1.5\,{\rm keV}$. This corresponds to a mass limit of $M_{\rm lim} = 2.42 \times 10^9\, h^{-1}\,{\rm M}_\odot$ and $M_{\rm min} = 0.5\, M_{\rm lim}$ given by equations derived by Wang & White (2007) and Lovell et al. (2014), respectively. These limits are indicated by dashed and dotted vertical lines in Fig. A1. Below these mass limits, the halo mass functions steepen significantly due to the emergence of spurious haloes.

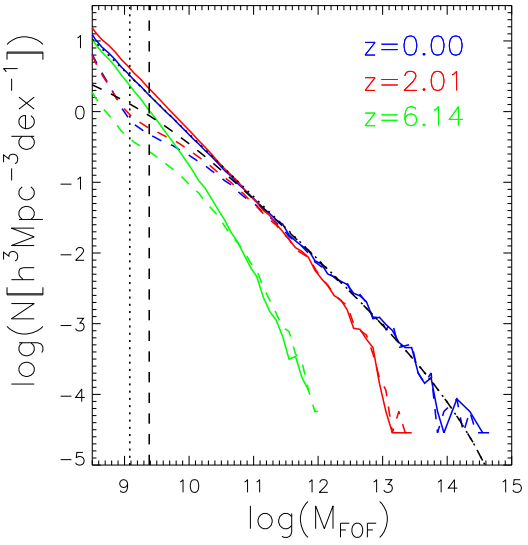

Figure A1. FOF group mass (total particle mass) function at three redshifts in the simulations. Solid lines denote the COLOR simulation and dashed lines COLOR-WARM. The vertical dashed and dotted lines are the limiting masses below which spurious haloes form in COLOR-WARM, given by Wang & White (2007) and Lovell et al. (2014).

APPENDIX B: BOX AND RESOLUTION EFFECTS

In this study, the simulation boxes we use are much smaller than the MS-W7 simulation that the GP14 model was calibrated with. In addition, the mass resolution of our simulations is about 100 times higher than that of MS-W7. Fig. B1 shows the galaxy SMFs at $z = 0$ of six COLOR-sized regions extracted from the MR-W7 simulation. We find that variations of up to 0.3 dex in galaxy abundance are expected due to cosmic variance.

Fig. B2 shows the SMFs of the GP14 model combined with MR-W7 and COLOR, while the dotted line is the SMF when COLOR trees have all the branches below the resolution of MR-W7 removed. Comparing the blue solid and blue dotted lines, we find that the effect of different mass resolutions on SMF is very small. The difference between the published GP14 model and that runs using merger trees from the COLOR simulation is mainly due to cosmic variance.

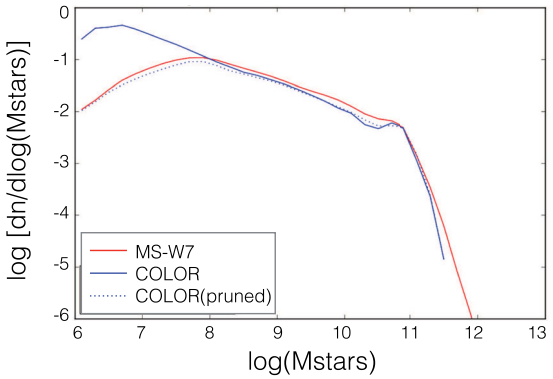

Figure B2. Stellar mass functions in the COLOR (blue line) and MR-W7 (red line), combined with GP14 model. The dotted line shows the result when the COLOR trees have all the branches below the resolution of MR-W7 removed.

APPENDIX C: THE RE-GP14 MODEL

For this study, we consider two galaxy formation models, one for COLOR (GP14) and a second for COLOR-WARM (Re-GP14), constructed to have very similar galaxy stellar mass functions at $z = 0$ for $10^9 < M_{\rm stars}/(h^{-1}\,{\rm M}_\odot) < 10^{11}$. Changing the parameters related to feedback is sufficient for the Re-GP14 model in COLOR-WARM to reproduce the stellar mass function from COLOR combined with GP14. The detailed changes of parameters from GP14 to Re-GP14 are listed in Table. C1. Both $\alpha_{\rm hot}$ and $V_{\rm hot,disc}$ are related to supernovae feedback, in that they determine the relation between the ejected cold gas mass and circular velocity $V_{\rm circ}$. $\alpha_{\rm hot}$ is the exponent of the relation (equation 1 of GP14):

$$\dot{M}_{\rm reheated} \propto (V_{\rm circ}/V_{\rm hot,disc})^{-\alpha_{\rm hot}}.$$

Table C1. Changes of parameters from the fiducial GP14 model to the retuned GP14 model, in order to match the galaxy stellar mass function at $z = 0$ for $10^9 < M_{\rm stars}/(h^{-1}\,{\rm M}_\odot) < 10^{11}$ of COLOR-WARM to that of COLOR.

Parameter	GP14	Re-GP14
$\alpha_{\rm hot}$	3.2	2.5
$V_{\rm hot,disc}$	425	575
$\alpha_{\rm cool}$	0.6	0.55

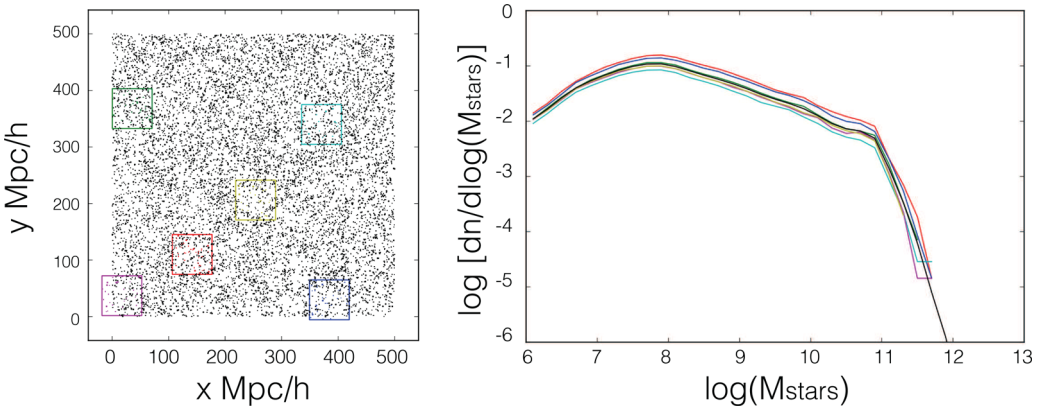

Figure B1. Left-hand panel: six random COLOR-sized regions (small coloured boxes) are extracted from MR-W7 (black dots denote the whole box). Right-hand panel: the galaxy stellar mass functions of the selected COLOR-sized regions (line colour corresponds to the box colour in the left-hand panel) combined with GP14 model. The black line is the stellar mass function of MR-W7 combined with the GP14 model.

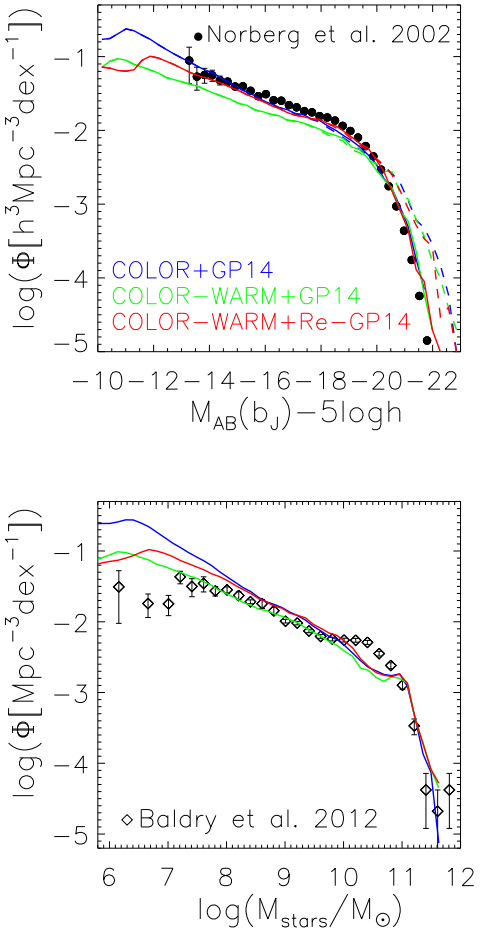

Figure C1. b_J-band luminosity functions and stellar mass functions of galaxies simulated. The symbols and lines in the panels are the same as in Fig. 1, whilst the additional green lines are the results of COLOR-WARM simulation combined with the original GP14 model. Note that the x-axis extends to lower stellar masses than in Fig. 1.

Decreasing $\alpha_{\rm hot}$ leads to lower feedback and ejected mass in low circular velocity galaxies and higher feedback in high circular velocity galaxies. $V_{\rm hot,disc}$ is the normalization of the relation for discs. The efficiency of supernovae feedback increases with larger $V_{\rm hot,disc}$. The normalization for bulges has not been changed.

Overall, supernovae feedback is weaker in low-mass galaxies, which leaves more cold gas available for star formation and therefore more efficient star formation in low-mass galaxies, and results in a larger amplitude for the luminosity and stellar mass functions. In massive galaxies, supernovae feedback is stronger.

$\alpha_{\rm cool}$ controls when a halo can be affected by AGN feedback (see equation 12 in Lacey et al. 2016). In Re-GP14, smaller values of $\alpha_{\rm cool}$ correspond to AGN feedback affecting fewer galaxies, which in turn alters the bright-end slope of the luminosity and stellar mass functions.

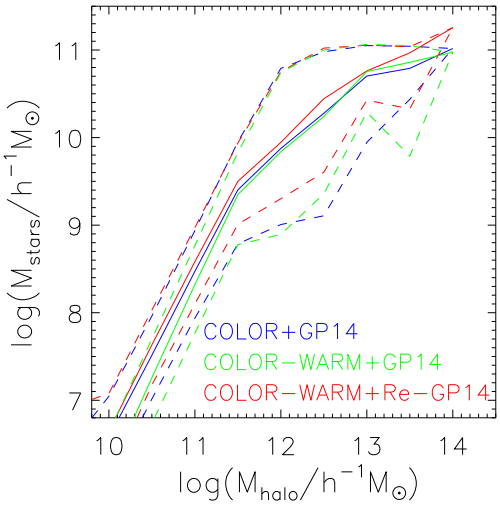

Figure C2. Median stellar mass–halo mass relations of central galaxies in the three models shown in the legend. Dashed lines indicate the region containing 90 per cent of the distribution for each relation.

Fig. C1 shows the b_J-band luminosity functions and stellar mass functions of galaxies in three catalogues at $z = 0$. Green lines show results from COLOR-WARM simulation combined with the original GP14 model without tuning of parameters. With the same semi-analytic models, COLOR-WARM produces fewer small galaxies because there are fewer low-mass haloes than in the COLOR simulation. Compared with the luminosity function results given by Bose et al. (2017), where the thermal mass of the WDM particle is assumed to be 3.3 keV for the WDM simulation, the difference between WDM and CDM is larger in our models, since the WDM particle mass assumed in our model, 1.5 keV, is warmer. The overall main effect of changing parameters from GP14 to Re-GP14 is that the number of low-mass/luminosity galaxies is larger, bringing galaxies in COLOR-WARM closer to the COLOR ones. The remaining difference on the faint/low-mass end at stellar masses less than $\sim 10^8\,{\rm M}_\odot$ is mainly due to the fact that there are fewer small haloes in COLOR-WARM, and thus not from the retuning of the galaxy formation model.

Fig. C2 shows the stellar mass–halo mass relations in the three models. With the same GP14 model, WDM produces lower stellar mass galaxies at fixed halo mass than CDM for haloes of mass $<10^{11.5}\,h^{-1}\,{\rm M}_\odot$. When combined with the Re-GP14 model, with weaker feedback effect, the stellar mass in COLOR-WARM becomes overall larger.

This paper has been typeset from a TEX/LATEX file prepared by the author.